Ice-Front Retreat Controls on Ocean Dynamics Under Larsen C Ice Shelf, Antarctica

Poinelli, M.; Nakayama, Y.; Larour, E.; Vizcaino, M.; Riva, R.

DOI
10.1029/2023GL104588

Publication date
2023

Document Version
Final published version

Published in
Geophysical Research Letters

Geophysical Research Letters

RESEARCH LETTER
10.1029/2023GL104588

Ice-Front Retreat Controls on Ocean Dynamics Under Larsen C Ice Shelf, Antarctica

M. Poinelli[1,2,3], Y. Nakayama[4], E. Larour[2], M. Vizcaino[3], and R. Riva[3]

[1]Department of Earth System Science, University of California, Irvine, Irvine, CA, USA, [2]Jet Propulsion Laboratory, California Institute of Technology, Pasadena, CA, USA, [3]Department of Geoscience and Remote Sensing, Delft University of Technology, Delft, The Netherlands, [4]Institute of Low Temperature Science, Hokkaido University, Sapporo, Japan

Key Points:

- We present ocean simulations under Larsen C in good agreement with local ocean, basal melt and sea-ice observations
- The removal of iceberg A-68 yields heat intrusion to increase by 30% causing melt around Gipps Ice Rise to double
- Ocean models need to consider ice-front retreat events and realistic ice-shelf geometry to accurately project sub-shelf ocean circulation

Supporting Information:

Supporting Information may be found in the online version of this article.

Correspondence to:

M. Poinelli,
mattia.poinelli@uci.edu

Citation:

Poinelli, M., Nakayama, Y., Larour, E., Vizcaino, M., & Riva, R. (2023). Ice-front retreat controls on ocean dynamics under Larsen C Ice Shelf, Antarctica. *Geophysical Research Letters*, *50*, e2023GL104588. https://doi.org/10.1029/2023GL104588

Received 19 MAY 2023
Accepted 31 AUG 2023

Abstract Iceberg A-68 separated from the Larsen C Ice Shelf in July 2017 and the impact of this event on the local ocean circulation has yet to be assessed. Here, we conduct numerical simulations of ocean dynamics near and below the ice shelf pre- and post-calving. Results agree with in situ and remote observations of the area as they indicate that basal melt is primarily controlled by wintertime sea-ice formation, which in turn produces High Salinity Shelf Water (HSSW). After the calving event, we simulate a 50% increase in HSSW intrusion under the ice shelf, enhancing ocean heat delivery by 30%. This results in doubling of the melt rate under Gipps Ice Rise, suggesting a positive feedback for further retreat that could destabilize the Larsen C Ice Shelf. Assessing the impact of ice-front retreat on the heat delivery under the ice is crucial to better understand ice-shelf dynamics in a warming environment.

Plain Language Summary In July 2017, the Larsen C Ice Shelf, Antarctica, calved one of the largest icebergs ever observed: A-68. The impact of this event on the ocean circulation near and below the ice remains unknown. Our simulations from an ocean model suggest that the iceberg separation may have led to increased ocean heat delivery under the ice, yielding more vigorous bottom melt.

1. Introduction

Most ice shelves in the eastern Antarctic Peninsula have either retreated significantly or disintegrated over the past few decades (Cook & Vaughan, 2010). The consequent loss of buttressing force resulted in up to an eight-fold increase in freshwater discharge from glaciers north of the Larsen C Ice Shelf, with an estimated sea-level rise equivalent of approximately 0.9 mm since 1979 (Rignot et al., 2004, 2019; Scambos et al., 2004). In July 2017, Larsen C calved one of the largest icebergs ever observed: A-68. This event did not completely destabilize the ice shelf but it brought the ice front into its furthest receded position observed so far. With further calving, the ice front may recede beyond the compressive arch, a mechanical threshold that could lead to irreversible retreat (Doake et al., 1998; Fuerst et al., 2016). Processes driving ice-front retreat require further understanding as consequences of climate warming become more evident.

After ice-shelf retreat events, the temporary ice front is often pinned by ice rises, rumples, islands, and shallow bathymetric features that buttress the ice flow (Thomas, 1979). Past studies suggest that ocean-induced ablation of thin ice around such critical pinning points is important for the ice-shelf stability. For the Larsen C Ice Shelf, basal melt surrounding pinning points such as the Gipps and Bawden Ice Rises (GIR, BIR, Figure 1) is thought to reactivate local rifts, potentially leading to calving events such as the event in 2017 (Borstad et al., 2013; P. R. Holland et al., 2009; Kulessa et al., 2014; Larour et al., 2021). However, pathways of ocean heat intrusion under Larsen C during and after the calving of iceberg A-68, along with the aftermath on basal melting around local pinning points, remain poorly understood. Long-term in situ data are sparse as persistent sea-ice makes these locations particularly inaccessible.

The current understanding of ocean circulation beneath and in front of Larsen C mostly revolves around the few available in situ observations, which have been investigated in combination with numerical models. Two expeditions in February 2002 and March 2019 detected warm (−1.5°C) modified Warm Deep Water (mWDW) near BIR (Hutchinson et al., 2020; Nicholls et al., 2004). During the summer, mWDW reaches Larsen C and mixes with High Salinity Shelf Water (HSSW), which forms at the ocean surface after strong winter sea-ice production (Nicholls et al., 2009). The resulting water mass—after heat from mWDW is redistributed via local mixing with cooler shelf waters—intrudes in the Larsen C ice cavity and flows toward the grounding line along the Kenyon

10.1029/2023GL104588

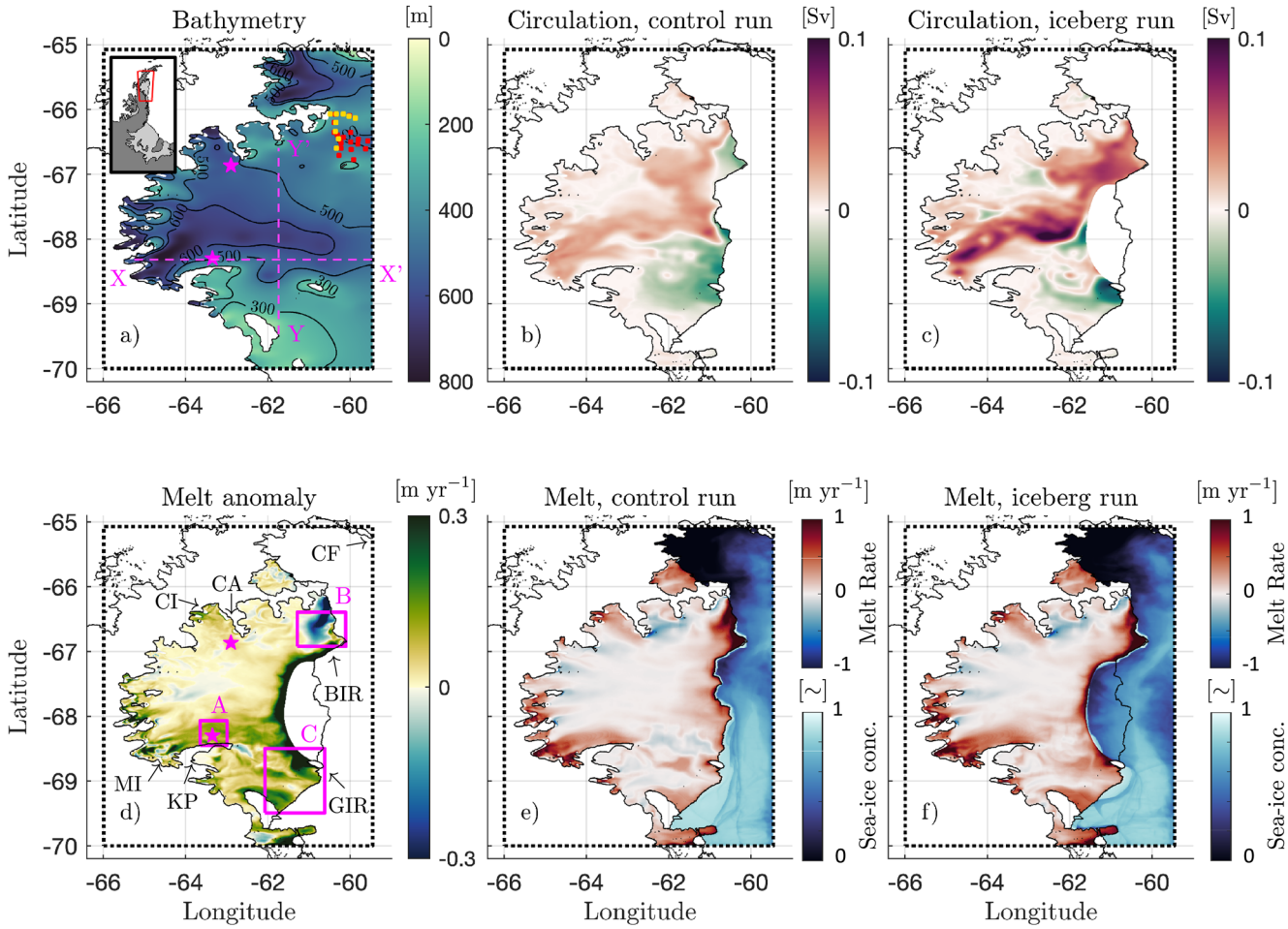

Figure 1. Model domain (dotted black box), integrated barotropic streamfunction, melt rate and sea-ice concentration. Magenta stars are the locations of drill sites after Nicholls et al. (2012). Yellow and red squares are the locations of CTD observations after Nicholls et al. (2004) and Hutchinson et al. (2020), respectively. (a) Bathymetry, both background colormap and contour lines. Magenta dashed lines are vertical cross-sections X-X' and Y-Y'. (b) Barotropic streamfunction in Sverdrup (Sv), control run. (c) Barotropic streamfunction, iceberg run. (d) Integrated melt anomaly as difference between integrated melt rate for iceberg (f) and control (e) runs. Streamfunction and melt patterns are calculated as temporal average between 1 January 2015 and 1 January 2017. Magenta boxes A, B, and C are key locations investigated in this paper, covering the survey area of Nicholls et al. (2012) and the shallow areas that coincide with the Bawden and Gipps Ice Rises, respectively. (f) and (e) also include monthly average of sea-ice concentration at the end of summer (March 2016), that is, when its concentration is the lowest. BIR: Bawden Ice Rise, GIR: Gipps Ice Rise, CA: Cape Alexander, CF: Cape Fairweather, CI: Cabinet Inlet, KP: Kenyon Peninsula, MI: Mobiloil Inlet.

Peninsula (Harrison et al., 2022; P. R. Holland et al., 2009; Hutchinson et al., 2020; Mueller et al., 2012). Data from hot-water boreholes drilled near the grounding line (magenta stars, Figure 1) in December 2011 showed that sampled water was at the local freezing point (−1.9°C), which excludes direct on-shelf intrusion of a "pure" (hence warmer) version of mWDW (Nicholls et al., 2012). As a consequence, the average basal melt near the grounding line is relatively low, that is, approximately 0.7 m yr^{-1} (Davis & Nicholls, 2019).

It is unknown if and how the calving of iceberg A-68 affected these sub-shelf circulation patterns. The impact of ice-front retreat and ice rifts on the dynamics of Antarctic ice shelves is only beginning to be explored (Bradley et al., 2022; Poinelli et al., 2023; Yoon et al., 2022). In this work, we use a regional ocean simulation of the Larsen C ice cavity at high-resolution to study sub-shelf ocean circulation and its effects on basal melt rates. We then investigate the impact of ice-front retreat on pathways of heat intrusion under the ice.

2. Methodology

2.1. Ocean Model

We use the Massachusetts Institute of Technology General Circulation Model (MITgcm) with thermodynamic ice shelf and dynamic/thermodynamic sea-ice (Losch, 2008; Losch et al., 2010). Basal ice-shelf melt is computed using the three-equation model (Hellmer & Olbers, 1989; D. M. Holland & Jenkins, 1999; Jenkins, 1991). Ocean, sea-ice, and ice-shelf parameters are nearly identical to those used by Nakayama et al. (2019). However, we calculate here coefficients of heat and salt transfer using drag laws and friction velocities based on a momentum-flux-derived drag coefficient $C_d = 0.0022$, which was obtained from in situ observations (Davis & Nicholls, 2019). Bed topography (Figure 1a) and ice-shelf geometry are interpolated from the state-of-the-art compilation BedMachine-V3 (Morlighem et al., 2020). Nominal horizontal and vertical grid spacing are set to 500 and 10 m, respectively, which constrain the step size of integration time to 30 s.

Boundary conditions are applied at the eastern and southern domain boundaries, while the northern boundary is closed and coincides with the seaward extension of Cape Fairweather. Summertime (December-March) boundary conditions of potential temperature and salinity (θ-S) are derived from available conductivity-temperature-depth (CTD) observations from the expedition of 2019 (Figure S1 in Supporting Information S1; Hutchinson et al., 2020). During the wintertime period (April-November), temperatures at the boundaries of the domain are maintained at a constant value of -1.9°C. Meanwhile, the salinity profile remains the same as during the summer season. We also apply tidal forcing as Dirichlet boundary conditions. Tidal amplitudes and phases are obtained from the data-assimilative barotropic tidal model of Padman et al. (2002). Realistic monthly-averaged surface forcing is interpolated on the model domain from numerically-analyzed atmospheric data from the ERA5 land reanalysis (Hersbach et al., 2020). Sea-ice concentration and thickness along the eastern and southern boundaries are interpolated from the coarse resolution global state estimate ECCO-LLC270 optimization (Zhang et al., 2018). Due to computational constraints, sea-ice velocities at the boundaries are directly calculated by surface fluxes forcing in the interior.

2.2. Experiments

We conduct two distinct experiments running over the same temporal span: from 1 January 2010 to 1 January 2017. In the first, we simulate ocean dynamics using the ice-shelf front prior to the calving of iceberg A-68 (control run). In the second, we use the ice-shelf front after the calving event, in which iceberg A-68 is removed from the model domain (iceberg run). Both simulations spin up for a period of 5 years under identical atmospheric and boundary forcing. The following analysis refers to model output after the spin-up, that is, between 1 January 2015 and 1 January 2017.

To investigate differences in sub-shelf circulation in the two experiments, we release two passive tracers on 1 January 2015, following the approach of Nakayama et al. (2017, 2021). Tracer `tr01` is restored to a unity value and released at the ocean surface as a proxy for HSSW concentration. The restoring time scale is one hour. A second tracer is released at the ice-shelf base at the same rate as melting occurs in order to track meltwater fraction (MWF).

3. Results

Model results of the control run are discussed in Section 3.1 and a brief comparison with available observations is in Section 3.2. Results of the iceberg run are in Section 3.3.

3.1. Ocean Circulation Prior to the Calving of Iceberg A-68

The control run simulates ocean conditions before the calving of iceberg A-68 (Figures 1, 2a–2c, 3a–3d, 4a–4d, Figures S2–S5 in Supporting Information S1). High sea-ice production is simulated near the ice front during the austral winter season between March and October, with polynya modeled in the north of the domain. As a result of loss of buoyancy in response to brine rejection from sea-ice formation, tracer `tr01` (as proxy for HSSW) convects to deeper layers and intrudes into the ice cavity (Movie S1).

Water in the ocean flows along lines of constant depth. In order to conserve potential vorticity, the flow entering the cavity is constrained by the presence of an ice front which acts as a barrier (Grosfeld et al., 1997). This abruptly reduces the water column thickness and curtails on-shelf intrusion. As a consequence, tracer `tr01` is channeled along three distinct bathymetric pathways (red arrows in Figure 2a). The most intense intrusion occurs around latitude 68°S and along the "southern trough" (a deep bathymetric feature documented in Brisbourne et al., 2020). Along this pathway, `tr01` sinks to the seabed in the open ocean and drains into the deep trough

10.1029/2023GL104588

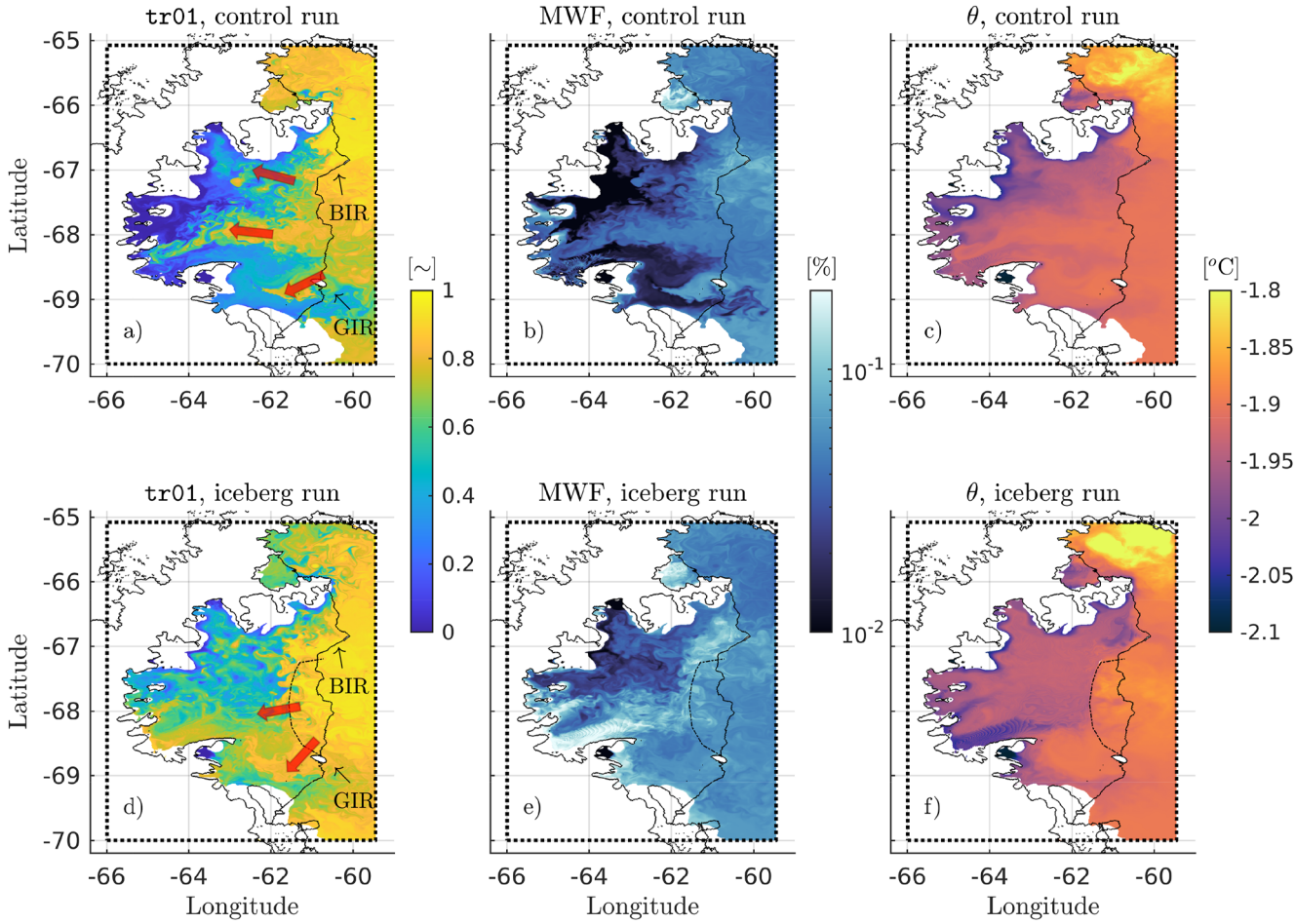

Figure 2. Simulated ocean conditions along the horizontal cross-section corresponding to isopycnal surface 27.90. (a) Concentration of passive tracer `tr01` as a snapshot of 1 January 2017. Red arrows show direction of the pathways of `tr01` intrusion. (b) Distribution of meltwater fraction (MWF) calculated on the same day. (c) Distribution of potential temperature as an average for December 2016. (d)–(f) are same as (a)–(c) but for the iceberg run.

toward the Mobiloil inlet. Second and third pathways occur around the two pinning points. Near GIR, ocean currents interact with thin ice, and the relatively flat seabed favors intrusion of `tr01`. Water that eventually enters the cavity wraps around the Kenyon Peninsula and reaches the Mobiloil inlet at the end of the second winter season. Similarly, `tr01` enters the cavity following the flat seabed near BIR. This water wraps around Cape Alexander and sinks toward the Cabinet inlet.

Due to the seasonal variability of sea-ice, the intrusion of `tr01` into the cavity occurs in pulses (Figure S6 in Supporting Information S1). During the first summer months, the model simulates sea-ice melting with the consequent freshening of surface water and `tr01` being confined in the mixed layer. At the beginning of the first winter, sea-ice production increases. Cumulative on-shelf intrusion of `tr01` accelerates in June 2015, stabilizes at the end of the first winter season, and remains constant throughout the summer. At the beginning of the second winter, `tr01` intrusion accelerates again and at the end of 2016, the cumulative on-shelf `tr01` volume is twice as much as at the end of 2015.

The intrusion of HSSW drives melting when this saline water interacts with the base of the ice shelf (Figures 1e and 2a). HSSW carries sufficient heat to melt ice as the freezing point decreases with increasing pressure. We find that the thermal driving pattern matches well the spatial distribution of melt rate, while changes in current velocity alone cannot explain the high simulated melt pattern at the grounding line (Figure S7 in Supporting Information S1). The model simulates three peaks of meltwater (Figure 2b) that correspond to the three intrusive pathways. The most significant peak, with MWF around ~0.1%, is found north of the Kenyon Peninsula (box A). Meltwater then flows north-northeast along the ice draft toward shallower layers and exits the cavity between latitude 68°S and 67°S. Other sources of meltwater are the GIR and BIR (boxes B and C), where the MWF is twice as high as in box A. Seasonal variability of melt rates in box A (Figure S6f in Supporting Information S1) further

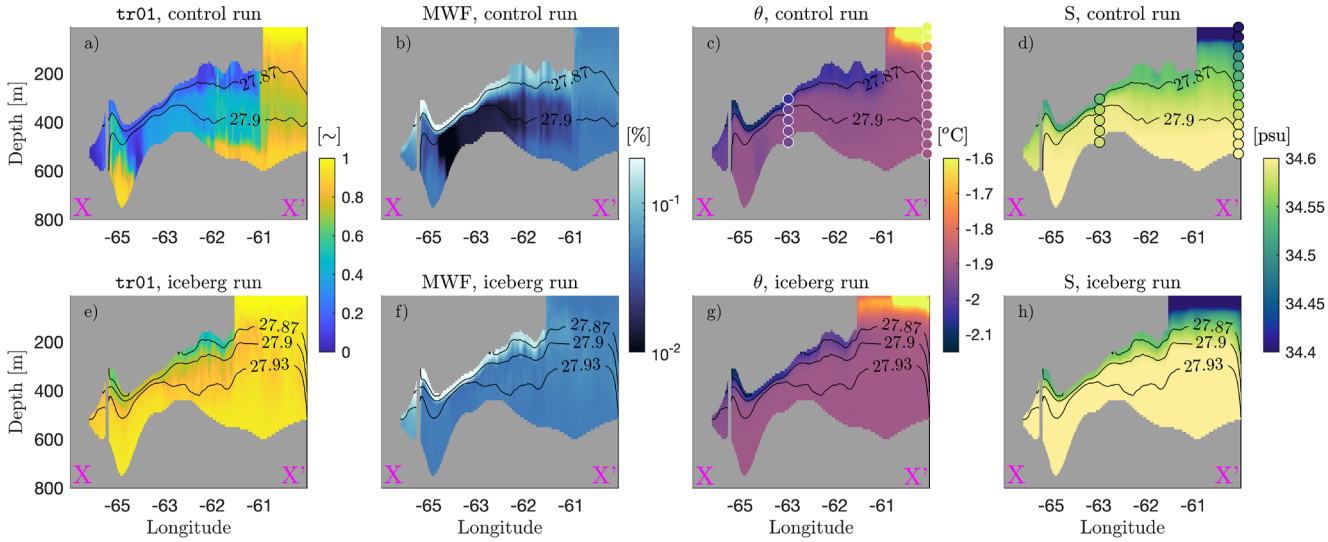

Figure 3. Simulated ocean conditions along vertical cross-sections X-X', which is aligned with the latitude of the south drill site. Black contour lines are isopycnal levels. (a), (b) Concentration of passive tracer `tr01` and meltwater fraction (MWF), respectively, as a snapshot for 1 January 2017 in the control run. (c), (d) Distribution of potential temperature and salinity in the control run as a monthly average for December 2016. Dotted markers are observation profiles of potential temperature (c) and salinity (d) after CTD data of Nicholls et al. (2012) (under the ice base) and Hutchinson et al. (2020) (open ocean). (e)–(h) are same as (a)–(d) but for the iceberg run.

shows a strong correlation ($R = 0.84$) with thermal driving (similar trends found under BIR and GIR, Figures S8 and S9 in Supporting Information S1). This confirms the dominance of ocean temperature on ice-shelf melting rather than ocean current speed ($R = 0.42$).

3.2. Model-Data Comparison

Simulated vertical profiles of potential temperature and salinity under the ice of the control run match well CTD observations (Figures 3c and 3d, 4c and 4d, Figures S1 and S5 in Supporting Information S1) accessed through the two drill sites in December 2011 (Nicholls et al., 2012). First, the model reproduces a layer of cold and fresh meltwater beneath the ice base around the local freezing temperature. Meltwater sits above denser and relatively warmer HSSW characterized by potential temperature around −1.9°C. Second, the modeled power spectrum shows

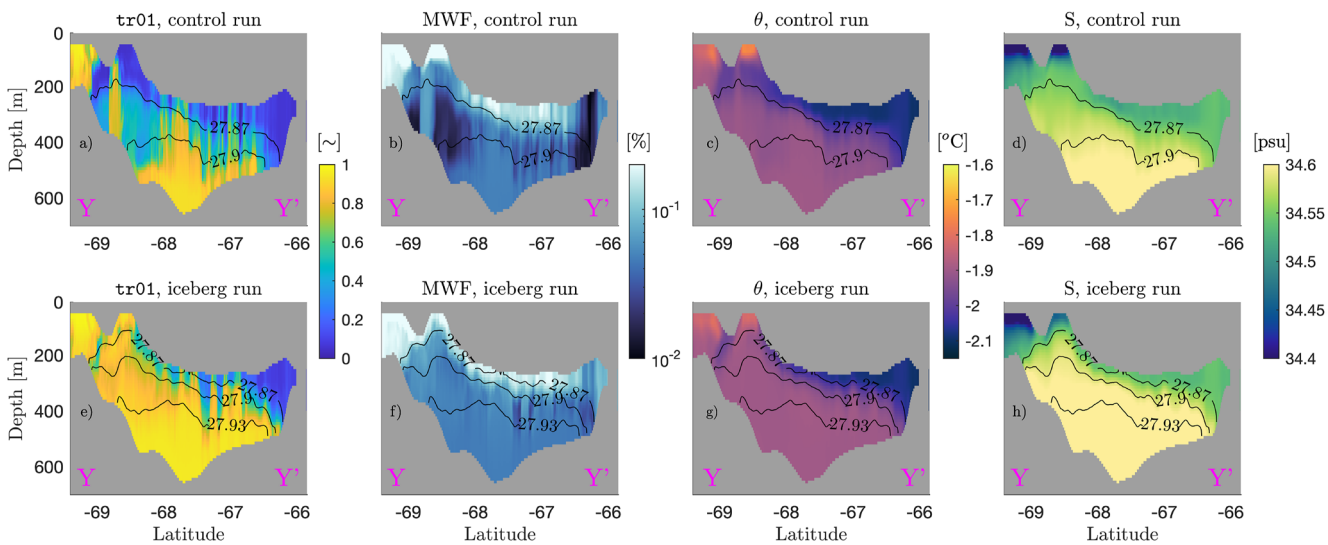

Figure 4. Simulated ocean conditions along vertical cross-section Y-Y'. Black contour lines are isopycnal levels. (a), (b) Concentration of passive tracer tr01 and meltwater fraction (MWF), respectively, as a snapshot for 1 January 2017 in the control run. (c), (d) Distribution of potential temperature and salinity in the control run as a monthly average for December 2016. (e)–(h) are same as (a)–(d) but for the iceberg run.

good agreement with in situ data acquired by a Nobska Modular Acoustic Velocity Sensor at the southern drill site (Figure S10 in Supporting Information S1) (Davis & Nicholls, 2019). Moreover, modeled sea-ice results for 2015 are in fairly good agreement ($R = 0.82$) with average sea-ice concentration in the Weddell Sea obtained via DMSP SSM/I-SSMIS passive microwave data (Figure S6 in Supporting Information S1) (DiGirolamo et al., 2022).

Simulated melt rate of the entire Larsen C Ice Shelf as an average of the two years of simulations is 0.11 m yr^{-1}. Average melt rate at the southern drill site (box A) is 0.18 m yr^{-1} and, in proximity of BIR and GIR (box B and C), it reaches 0.46 and 0.11 m yr^{-1}, respectively. The total ice-shelf melt rate average is in good agreement with 0.17 m yr^{-1}, estimated with altimetry observations spanning the same period (Adusumilli et al., 2018). At box A, in situ data (0.70 m yr^{-1}, Davis & Nicholls, 2019) and altimetry-derived measurements (0.36 m yr^{-1}, Adusumilli et al., 2018) are underestimated by the model. At boxes B and C, calculated melt is in reasonable alignment with altimetry-derived estimations of the two pinning points (1.11 and 0.36 m yr^{-1}, respectively).

3.3. Ocean Circulation After the Calving of Iceberg A-68

The iceberg run simulates ocean conditions after the calving of iceberg A-68 (Figures 1, 2d–2f, 3e–3h, 4e–4h, Figures S2–S5 in Supporting Information S1). The removal of iceberg A-68 from the ice-shelf geometry substantially alters the pathways through which ocean water intrudes and distributes heat beneath the ice by means of two processes. First, the retreat event results in the ice front migrating westward. This leads to polynya near the ice shelf also in the southern section of the model domain, while, in the control run, sea-ice presence in this area was more stable. Second, the removal of a substantial portion of ice, combined with the deeper bathymetry, increases the thickness of the water column along the new ice front with respect to the pre-calving conditions.

The aforementioned processes result in a two-fold effect. (a) An enhanced HSSW production along the new margin, which is a direct results of an increase in the number of polynya days during the two years of simulations. (b) A thicker water column along the ice front, which weakens the potential vorticity barrier caused by the ice shelf. As a consequence, these processes favor a widespread and more intense on-shelf intrusion of `tr01` with respect to the control run.

In the iceberg run, there are notable changes in the sinking behavior of `tr01` and the intrusion pattern along the southern trough compared to the control run. Instead of sinking primarily along the southern trough as observed in the latter, `tr01` sinks along the entire western edge of iceberg A-68 in the former. This sinking and intrusion are most pronounced south of latitude 67°S (Figure 2d), aligning with the new peaks of sea-ice production in the southern section of the model domain as well as the thicker water column along the ice front in the south. As a consequence, the overall intrusion of `tr01` below GIR is much stronger in the iceberg run, and the tracer reaches the western-most extensions of the ice-shelf cavity near the Mobiloil inlet after only a single winter season since the initial release (Movie S1).

Similar to the control run, the intrusion of HSSW occurs in pulses. `tr01` intrusion accelerates at the beginning of each winter season and stabilizes during the summer months when the model simulate sea-ice melting. However, in comparison to the control run, the iceberg run shows that the total on-shelf intrusion of `tr01` increases by 50% while heat transport toward the grounding line increases by 30% (Figures S6c and S6d in Supporting Information S1), due to the processes explained above. Consequently, the total integrated melt rate is 73% higher in the iceberg run, while the largest increase is concentrated south of latitude 68°S (Figures S6, S8, and S9 in Supporting Information S1). In particular, basal melt below GIR (calculated over box C) increases by 113% and the area north of Kenyon Peninsula, in proximity of the south drill site (calculated over box A) experiences a 54% increase. In contrast, basal melt around BIR (calculated over box B) decreases by 12%. While the basal melt increase south of latitude 68°S is a direct result of a stronger HSSW intrusion after ice-front retreat, the decrease of melt under BIR is a consequence of an enhanced northward flow of meltwater from the Mobiloil inlet. In comparison to the control run, meltwater flows more northward and along the new ice front and cools the ambient water under the ice in proximity of BIR (Figures 2e and 2f), curtailing local melt.

4. Discussion

Past studies delineated two future scenarios that would destabilize the Larsen C Ice Shelf and precondition its collapse (e.g., Doake et al., 1998; P. R. Holland et al., 2015; Jansen et al., 2013): (a) ungrounding of ice near BIR and GIR pinning points and (b) ice-front retreat beyond the compressive arch. Our simulations suggest that the calving event of 2017 may have redistributed ocean heat delivery under the ice base with an estimated doubling of

basal melt around GIR. This is particularly important as sustained thinning in this area has a two-fold effect. First, it may lead to ungrounding the ice shelf from the shallow bathymetry, with the consequent acceleration of the ice flow (Borstad et al., 2013). Second, it may re-activate dormant rifts, which could then lead to further ice-front retreat, similar to the event of 2017 (P. R. Holland et al., 2009; Larour et al., 2021). This positive feedback for further ice-shelf retreat after calving events is worthy of further investigation in order to accurately estimate the evolution and the impact of global sea level of the largest remaining ice shelf in the Antarctic Peninsula.

Our results build understanding on the need to consider updated ice-shelf margin geometry to accurately project ocean circulation below the ice. A recent study has demonstrated that ice-front retreat can have significant implications for the intrusion of warm Circumpolar Deep Water into the Pine Island Glacier cavity in the Amundsen Sea (Yoon et al., 2022). Here, our results show that calving events can also impact the mechanisms of HSSW intrusion under cold water ice shelves, which is the dominant driver of their basal ablation. In order to extend these results to other ice shelves, it is important to note that, rather than the physical retreat of the ice front alone, it is the overall hydrography of the post-calving condition that plays a crucial role in delivering heat toward the grounding line. For instance, the presence of bathymetric ridges (absent in the case of Larsen C) and the ice-front retreat beyond their location was shown to determine the actual extent of off-shelf water intrusion in the Pine Island Glacier cavity (Bradley et al., 2022).

A limitation of our simulations is the lack of large-scale ocean circulation in the Weddell Sea, as our lateral ocean boundary conditions are only based on barotropic tidal forcing. For example, our model is unable to account for the presence of relatively warm mWDW documented near BIR (Hutchinson et al., 2020; Nicholls et al., 2004), which could substantially increase the simulated basal melt. Furthermore, we do not consider the impact of frazil ice crystals, which accumulate under Antarctic ice shelves and form marine ice bodies. Under Larsen C, the thickness of marine ice is estimated to be up to a third to half of the ice-shelf depth, in agreement with numerical models (P. R. Holland et al., 2009; McGrath et al., 2014; Harrison et al., 2022). The role of frazil accretion in the form of such thick layers of marine ice is well documented for the ice flow, but the impact of accreted ice on the on-shelf heat intrusion is not fully understood (Jansen et al., 2013; Kulessa et al., 2014). Further numerical simulations need to take into account realistic ocean forcing and to investigate its impact on frazil ice accretion under weakly-stratified ice shelves such as Larsen C, where marine ice is abundant.

Finally, we find that ocean temperature has a stronger impact on ice-shelf melting compared to current speed. This is in contrast of what has been modeled for warm water ice shelves (e.g., Pine Island and Thwaites Ice Shelves, Nakayama et al., 2019) and suggests a distinctive characteristic specific to cold water ice shelves. As a response to ongoing and future climate change, warm water could be transported progressively closer to large cold water ice shelves in the Weddell Sea (Darelius et al., 2016; Hellmer et al., 2012), most likely in the form of mWDW. Calving events could facilitate the intrusion of relatively warm mWDW under the ice and therefore increase their basal melt. Although there have been no direct observations of mWDW intrusion under the Larsen C Ice Shelf to date, our simulations emphasize the importance of additional observations and modeling efforts to monitor the arrival and impact of warm coastal currents beneath this and other cold water ice shelves.

5. Conclusions

We present high-resolution ocean simulations nearby and below the Larsen C Ice Shelf before and after the calving of iceberg A-68. Results from the post-calving run suggest that the removal of iceberg A-68 yields High Salinity Shelf Water and ocean heat intrusion to increase by 50% and 30%, respectively. Particularly, this results in basal melt around the Gipps Ice Rise to double. Enhanced thinning around this pinning point can lead to further rifting and calving, ultimately compromising the mechanical stability of the ice shelf. Consequently, our results suggest a positive feedback loop for further ice-front retreat. Our findings underscore the critical importance of considering updated ice-shelf margin geometry when aiming to understand the processes controlling ocean heat intrusion beneath ice shelves. By extension, this knowledge is crucial for accurately quantifying basal ablation and thus the contribution of Antarctica to global sea-level rise, as the effects of climate warming become more evident.

Data Availability Statement

The Massachusetts Institute of Technology general circulation model is an open source numerical model freely available on Github at https://github.com/MITgcm/MITgcm (checkpoint 66j). Model code, input and results are available at https://ecco.jpl.nasa.gov/drive/files/ECCO2/High_res_LarsenC (registration is required to access the

data). Model code and input are also available on Zenodo/Github at https://doi.org/10.5281/zenodo.8336591 and https://github.com/MITgcm-contrib/ecco_polar_regional.

Acknowledgments
Part of this work was carried out at the Jet Propulsion Laboratory, California Institute of Technology, under a contract with the National Aeronautics and Space Administration (NASA). High-end computing resources were provided by the NASA Advanced Supercomputing Division. Color schemes are from Thyng et al. (2016). MP thanks Keith Nicholls for kindly providing data collected during the RRS JCR campaign, Chad Greene for the help in visualizing model output via AMT (Greene et al., 2017) and Michael Schodlok for the support with the initial model set-up. YN was supported by the Grants-in-Aid for Scientific Research (21K13989) of the Japanese Ministry of Education, Culture, Sports, Science, and Technology and by the Inoue Science Research Award from the Inoue Science Foundation.

References

Adusumilli, S., Fricker, H. A., Siegfried, M. R., Padman, L., Paolo, F. S., & Ligtenberg, S. R. M. (2018). Variable basal melt rates of Antarctic Peninsula ice shelves, 1994–2016. *Geophysical Research Letters*, *40*(9), 4086–4095. https://doi.org/10.1002/2017GL076652

Borstad, C., Rignot, E., Mouginot, J., & Schodlok, M. (2013). Creep deformation and buttressing capacity of damaged ice shelves: Theory and application to Larsen C ice shelf. *The Cryosphere*, *7*(6), 1931–1947. https://doi.org/10.5194/tc-7-1931-2013

Bradley, A. T., Bett, D. T., Dutrieux, P., De Rydt, J., & Holland, P. R. (2022). The influence of pine island ice shelf calving on basal melting. *Journal of Geophysical Research: Oceans*, *127*(9), e2022JC018621. https://doi.org/10.1029/2022JC018621

Brisbourne, A., Kulessa, B., Hudson, T., Harrison, L., Holland, P., Luckman, A., et al. (2020). An updated seabed bathymetry beneath Larsen C ice shelf, Antarctic Peninsula. *Earth System Science Data*, *12*(2), 887–896. https://doi.org/10.5194/essd-12-887-2020

Cook, A. J., & Vaughan, D. G. (2010). Overview of areal changes of the ice shelves on the Antarctic Peninsula over the past 50 years. *Geophysical Research Letters*, *4*(1), 77–98. https://doi.org/10.5194/tc-4-77-2010

Darelius, E., Fer, I., & Nicholls, K. W. (2016). Observed vulnerability of Filchner-Ronne Ice Shelf to wind-driven inflow of warm deep water. *Nature Communications*, *7*(1), 12300. https://doi.org/10.1038/ncomms12300

Davis, P. E. D., & Nicholls, K. W. (2019). Turbulence observations beneath Larsen C ice shelf, Antarctica. *Journal of Geophysical Research: Oceans*, *124*(8), 5529–5550. https://doi.org/10.1029/2019JC015164

DiGirolamo, N., Parkinson, C. L., Cavalieri, D. J., Gloersen, P., & Zwally, H. J. (2022). *Sea ice concentrations from Nimbus-7 SMMR and DMSP SSM/I-SSMIS passive microwave data, version 2*. NASA National Snow and Ice Data Center Distributed Active Archive Center. https://doi.org/10.5067/MPYG15WAA4WX

Doake, C. S. M., Corr, H., Rott, H., Skvarca, P., & Young, N. (1998). Breakup and conditions for stability of the northern Larsen ice shelf, Antarctica. *Nature*, *398*(6669), 778–780. https://doi.org/10.1038/35832

Fuerst, J. J., Durand, G., Gillet-Chaulet, F., Tavard, L., Rankl, M., Braun, M., & Gagliardini, O. (2016). The safety band of Antarctic ice shelves. *Nature Climate Change*, *6*(5), 479–482. https://doi.org/10.1038/nclimate2912

Greene, C. A., Gwyther, D. E., & Blankenship, D. D. (2017). Antarctic mapping tools for Matlab. *Computers & Geosciences*, *104*, 151–157. https://doi.org/10.1016/j.cageo.2016.08.003

Grosfeld, K., Gerdes, R., & Determan, J. (1997). Thermohaline circulation and interaction between ice shelf cavities and the adjacent open ocean. *Journal of Geophysical Research*, *102*(C7), 15595–15610. https://doi.org/10.1029/97JC00891

Harrison, L. C., Holland, P. R., Heywood, K. J., Nicholls, K. W., & Brisbourne, A. M. (2022). Sensitivity of melting, freezing and marine ice beneath Larsen C ice shelf to changes in ocean forcing. *Geophysical Research Letters*, *49*(4), 18–27. https://doi.org/10.1029/2021GL096914

Hellmer, H. H., Kauker, F., Timmermann, R., Determann, J., & Rae, J. (2012). Twenty-first-century warming of a large Antarctic ice-shelf cavity by a redirected coastal current. *Nature*, *485*(7397), 225–228. https://doi.org/10.1038/nature11064

Hellmer, H. H., & Olbers, D. J. (1989). A two-dimensional model of the thermohaline circulation under an ice shelf. *Antarctic Science*, *1*(4), 325–336. https://doi.org/10.1017/S0954102089000490

Hersbach, H., Bell, B., Berrisford, P., Hirahara, S., Horányi, A., Muñoz-Sabater, J., et al. (2020). The ERA5 global reanalysis. *Quarterly Journal of the Royal Meteorological Society*, *146*(730), 1999–2049. https://doi.org/10.1002/qj.3803

Holland, D. M., & Jenkins, A. (1999). Modeling thermodynamic ice-ocean interactions at the base of an ice shelf. *Journal of Physical Oceanography*, *29*(8), 1787–1800. https://doi.org/10.1175/1520-0485(1999)029⟨1787:MTIOIA⟩2.0.CO;2

Holland, P. R., Brisbourne, A., Corr, H. F. J., McGrath, D., Purdon, J., Paden, K., et al. (2015). Oceanic and atmospheric forcing of Larsen C Ice-Shelf thinning. *The Cryosphere*, *9*(3), 616–620. https://doi.org/10.5194/tc-9-1005-2015

Holland, P. R., Corr, H. F. J., Vaughan, D. G., Jenkins, A., & Skvarca, P. (2009). Marine ice in Larsen ice shelf. *Geophysical Research Letters*, *36*(11), L11604. https://doi.org/10.1029/2009GL038162

Hutchinson, K., Deshayes, J., Sallee, J., Dowdeswell, J. A., de Lavergne, C., Ansorge, I., et al. (2020). Water mass characteristics and distribution adjacent to Larsen C Ice Shelf, Antarctica. *Journal of Geophysical Research: Oceans*, *125*(4), e2019JC015855. https://doi.org/10.1029/2019JC015855

Jansen, D., Luckman, A. J., Kulessa, B., Holland, P. R., & King, E. C. (2013). Marine ice formation in a suture zone on the Larsen C Ice Shelf and its influence on ice shelf dynamics. *Journal of Geophysical Research: Earth Surface*, *118*(3), 1628–1640. https://doi.org/10.1002/jgrf.20120

Jenkins, A. (1991). A one-dimensional model of ice shelf-ocean interaction. *Journal of Geophysical Research*, *96*(11), 20671–20677. https://doi.org/10.1029/91JC01842

Kulessa, B., Jansen, D., Luckman, A. J., King, E. C., & Sammonds, P. R. (2014). Marine ice regulates the future stability of a large Antarctic ice shelf. *Nature Communications*, *5*(1), 3707. https://doi.org/10.1038/ncomms4707

Larour, E., Rignot, E., Poinelli, M., & Scheuchl, B. (2021). Processes controlling the rifting of Larsen C Ice Shelf, Antarctica, prior to the calving of iceberg A68. *PNAS*, *118*(40), 1–8. https://doi.org/10.1073/pnas.2105080118

Losch, M. (2008). Modeling ice shelf cavities in a z coordinate ocean general circulation model. *Journal of Geophysical Research*, *113*(C8), C08043. https://doi.org/10.1029/2007JC004368

Losch, M., Menemenlis, D., Campin, J.-M., Heimback, P., & Hill, C. (2010). On the formulation of sea-ice models. Part 1: Effects of different solver implementations and parameterizations. *Ocean Modelling*, *33*(1–2), 129–144. https://doi.org/10.1016/j.ocemod.2009.12.008

McGrath, D., Steffen, K., Holland, P. R., Scambos, T., Rajaram, H., Abdalati, W., & Rignot, E. (2014). The structure and effect of suture zones in the Larsen C Ice Shelf, Antarctica. *Journal of Geophysical Research: Earth Surface*, *119*(3), 588–602. https://doi.org/10.1002/2013JF002935

Morlighem, M., Rignot, E., Binder, T., Blankenship, D., Drews, R., Eagles, G., et al. (2020). Deep glacial troughs and stabilizing ridges unveiled beneath the margins of the Antarctic ice sheet. *Nature Geoscience*, *13*(2), 132–137. https://doi.org/10.1038/s41561-019-0510-8

Mueller, R. D., Padman, L., Dinniman, M. S., Erofeeva, S. Y., Fricker, H. A., & King, M. A. (2012). Impact of tide-topography interactions on basal melting of Larsen C Ice Shelf, Antarctica. *Journal of Geophysical Research*, *117*(C5), C05005. https://doi.org/10.1029/2011JC007263

Nakayama, Y., Cai, C., & Seroussi, H. (2021). Impact of subglacial freshwater discharge on Pine Island ice shelf. *Geophysical Research Letters*, *48*(18), e2021GL093923. https://doi.org/10.1029/2021GL093923

Nakayama, Y., Manucharyan, G., Zhang, H., Dutrieux, P., Torres, H. S., Klein, P., et al. (2019). Pathways of ocean heat towards Pine Island and Thwaites grounding lines. *Scientific Reports*, *9*(1), 16649. https://doi.org/10.1038/s41598-019-53190-6

Nakayama, Y., Menemenlis, D., Schodlok, M., & Rignot, E. (2017). Amundsen and Bellingshausen Seas simulation with optimized ocean, sea ice, and thermodynamic ice shelf model parameters. *Geophysical Research Letters*, *122*(122), 6180–6195. https://doi.org/10.1002/2016JC012538

Nicholls, K. W., Makinson, K., & Venables, E. J. (2012). Ocean circulation beneath Larsen C ice shelf, Antarctica from in situ observations. *Geophysical Research Letters*, *39*(19), 995–1008. https://doi.org/10.1029/2012GL053187

Nicholls, K. W., Østerhus, S., Makinson, K., Gammelsrød, T., & Fahrbach, E. (2009). Ice-ocean processes over the continental shelf of the southern Weddell Sea, Antarctica: A review. *Reviews of Geophysics*, *47*(3), RG3003. https://doi.org/10.1029/2007RG000250

Nicholls, K. W., Pudsey, C. J., & Morris, P. (2004). Summertime water masses off the northern Larsen C ice shelf, Antarctica. *Geophysical Research Letters*, *31*(9), L09309. https://doi.org/10.1029/2004GL019924

Padman, L., Fricker, H. A., Coleman, R., Howard, S., & Erofeeva, L. (2002). A new tidal model for the Antarctic ice shelves and seas. *Annals of Glaciology*, *34*, 247–254. https://doi.org/10.3189/172756402781817752

Poinelli, M., Schodlok, M., Larour, E., Vizcaino, M., & Riva, R. (2023). Can rifts alter ocean dynamics beneath ice shelves? *The Cryosphere*, *17*, 2261–2283. https://doi.org/10.5194/tc-17-2261-2023

Rignot, E., Casassa, G., Gogineni, P., Krabill, W., Rivera, A., & Thomas, R. (2004). Accelerated ice discharge from the Antarctic Peninsula following the collapse of Larsen B ice shelf. *Geophysical Research Letters*, *31*(18), L18401. https://doi.org/10.1029/2004GL020697

Rignot, E., Mouginot, J., Scheuchl, B., van den Broeke, M., van Wessem, M. J., & Morlighem, M. (2019). Four decades of Antarctic ice sheet mass balance from 1979–2017. *Proceedings of the National Academy of Sciences*, *116*(4), 1095–1103. https://doi.org/10.1073/pnas.1812883116

Scambos, T. A., Bohlander, J. A., Shuman, C. A., & Skvarca, P. (2004). Glacier acceleration and thinning after ice shelf collapse in the Larsen B embayment, Antarctica. *Geophysical Research Letters*, *31*(18), L18402. https://doi.org/10.1029/2004GL020670

Thomas, R. H. (1979). Ice shelves: A review. *Journal of Glaciology*, *24*(90), 273–286. https://doi.org/10.3189/S0022143000014799

Thyng, K., Greene, C., Hetland, R., Zimmerle, H. M., & DiMarco, S. (2016). True colors of oceanography: Guidelines for effective and accurate colormap selection. *Oceanography*, *29*(3), 9–13. https://doi.org/10.5670/oceanog.2016.66

Yoon, S.-T., Lee, W. S., Nam, S., Lee, C.-K., Yun, S., Heywood, K., et al. (2022). Ice front retreat reconfigures meltwater-driven gyres modulating ocean heat delivery to an Antarctic ice shelf. *Nature Communications*, *13*(1), 306. https://doi.org/10.1038/s41467-022-27968-8

Zhang, H., Menemenlis, D., & Fenty, I. (2018). ECCO LLC270 ocean-ice state estimate. Retrieved from http://hdl.handle.net/1721.1/119821